Journal of Materials Chemistry A

S-Doped Ni(OH)2 Nano-Electrocatalyst Confined in Semiconductor Zeolite with Enhanced Oxygen Evolution Activity

Journal:	*Journal of Materials Chemistry A*
Manuscript ID	TA-ART-01-2020-000547.R2
Article Type:	Paper
Date Submitted by the Author:	15-May-2020
Complete List of Authors:	Hu, Dandan; Soochow University, College of Chemistry, Chemical Engineering and Materials Science Wang, Xiang; Soochow University, College of Chemistry, Chemical Engineering and Materials Science Chen, Xitong; University of California Riverside, Chemistry Wang, Yanxiang; University of California Riverside, materials science and engineering program Hong, Anh; University of California Riverside, Chemistry Zhong, Jun; Soochow University, Institute of Functional Nano & Soft Materials Bu, Xianhui; California State University Long Beach, Dept of Chemistry and Biochemistry Feng, Pingyun; University of California Riverside, Department of Chemistry Wu, Tao; Soochow University, College of Chemistry, Chemical Engineering and Materials Science

ARTICLE

S-Doped $Ni(OH)_2$ Nano-Electrocatalyst Confined in Semiconductor Zeolite with Enhanced Oxygen Evolution Activity

Received 00th January 20xx,
Accepted 00th January 20xx

DOI: 10.1039/x0xx00000x

Dandan Hu,[a,b] Xiang Wang,[a] Xitong Chen,[b] Yanxiang Wang,[b] Anh N. Hong,[b] Jun Zhong,[c] Xianhui Bu,[d] Pingyun Feng*[,b] and Tao Wu*[,a]

Low-cost $Ni(OH)_2$-based nanomaterials with various structures and morphologies are promising catalysts for efficient oxygen evolution reactions (OERs). However, homogenous $Ni(OH)_2$ nanomaterials with abundant active sites suffer from low conductivity and easy aggregation, resulting in low catalytic activity and stability. Here, we report a new synthetic method capable of generating abundant and confined S-doped β–$Ni(OH)_2$ nanoparticles (NPs) (3~5 nm) within a 3D semiconductor substrate, metal-chalcogenide semiconductor zeolite (CSZ). This method operates via sequential fluoride-assisted cationic stripping and in-situ $Ni(OH)_2$ generation and is demonstrated here as an effective method to synthesize Ni^{2+}-containing CSZ that are known to defy direct synthesis. The resulting composite (denoted $Ni(OH)_2$ NPs@CSZ) exhibited excellent OER performance with a very low overpotential of only 212 mV at a current density of 10 $mA{\cdot}cm^{-2}$ in O_2-saturated 1 M KOH solution, and low Tafel slope of 64.2 $mV{\cdot}dec^{-1}$, which is superior to that of benchmark IrO_2. DFT calculations indicate that the interaction between the embedded $Ni(OH)_2$ NPs and the dopant, S^{2-}, from the host CSZ played a crucial role in improving OER performance. This work provides a new path for developing high-performance $Ni(OH)_2$-based OER catalysts and may also serve as a general approach for loading large amounts of other catalytically active NPs into semiconducting open frameworks to further optimize electrocatalytic performance.

INTRODUCTION

Oxygen evolution reaction (OER) is generally identified as the rate-limiting step in water spliting for generating clean energy due to the sluggish kinetics involved with multistep proton-coupled electron transfer.[1-3] Although noble-metal oxide based materials (IrO_2 and RuO_2) are regarded as highly active catalysts for OER, the high cost and scarcity restrict their large-scale applications.[4-6] Therefore, in recent years, some abundant and low-cost 3d metal-based materials (Ni, Fe, Co, Mn *ect.*) with increasing activity and stability have been extensively explored and expected to replace noble-metal catalysts.[7-18] Among them, $Ni(OH)_2$ with various structures and morphologies were chosen as promising catalysts for highly-efficient OER because the high oxidation state of $Ni^{III/IV}$ in $Ni(OH)_2$-based materials can directly serve as active species in OER process.[19-23] Currently, there are two main strategies used for improving materials catalytic activity. The first strategy is to dope metal (W, Fe and Co) or nonmetal (B, P and F) ions in $Ni(OH)_2$-based catalysts.[24-31] Such type of dopants are capable of effectively regulating host conductivity and electronic structure of active sites, generating active bonding sites, and even providing vacant d orbitals to adsorb more water and OH^- groups, which greatly improve OER activity.[25, 29] Generally, most catalytic reaction occurs on the surface of catalysts, which demonstrates that the catalytic activities are largely depended on the geometric structure.[19, 22] Therefore, the second strategy is on the fabrication of various nanostructured $Ni(OH)_2$, such as nanosheeets, nanoarrays, hollow nanosponges and even nanoparticles *ect.*.[19, 22, 32, 33] In essence, both strategies aim to improve intrinsic activity of $Ni(OH)_2$ through generating more active sites and increasing contact area between catalysts and reactants, respectively. Obviously, nanosized $Ni(OH)_2$ particles, especially ultrasmall NPs, are considered as promising materials.[34] However, such nanosized $Ni(OH)_2$ NPs suffer from poor electronic conductivity and easy aggregation.[22] Incorporating these NPs into suitable conducting or semiconducting substrates not only increases the conductivity and charge transfer, but also effectively avoids the aggregation of NPs.[22, 35] For instance, Qu *et al.* embeded $Ni(OH)_2$ NPs (4.9~6.7 nm) in water-insoluble organic conductor (TCNQ) via anode oxidation for improving OER.[22] The formed $Ni(OH)_2$-TCNQ/CF displayed OER activity ($\eta_{50} = 322$ mV) similar to that of RuO_2.

Metal-chalcogenide semiconductor zeolites (CSZ) used here possess 3D uniform porosity, atomically ordered structure, large surface area as well as chemical and water stability. In addition, the sulfur-rich surface, would allow them serve as the special substrates in host-guest chemistry.[36-38] Theoretically, the unique structure features in CSZ may not only provide space for the confinement of $Ni(OH)_2$ NPs and

[a] *College of Chemistry, Chemical Engineering and Materials Science, Soochow University, Suzhou 215123, China*
[b] *Department of Chemistry, University of California, Riverside, California 92521, USA*
[c] *Institute of Functional Nano & Soft Materials (FUNSOM), Soochow University, Suzhou 215123, China*
[d] *Department of Chemistry and Biochemistry, California State University, Long Beach, California 90840, USA*
** Corresponding authors' E-mail addresses: wutao@suda.edu.cn; pingyun.feng@ucr.edu*

contribute to the effective contact and rapid interfacial electron-charge transfer, but also avoid the possible aggregation of $Ni(OH)_2$ NPs.[39, 40] Compared with other substrates, the characteristic of partially charged sulfur-rich surface of CSZ may increase the interaction between the confined $Ni(OH)_2$ NPs and host, and change the surrounding electronic structure of active sites.[27] However, due to the limitation on the size of the pores and charge density, it is rather difficult to embed abundant $Ni(OH)_2$ NPs in the nanocage of CSZ *via* traditional *in-situ* synthesis or post-synthetic method.

We here present a facile, ingenious and effective strategy, *i.e.* sequential fluoride-assisted cationic stripping and *in-situ* generation method, to construct $Ni(OH)_2$ NPs@CSZ nanocomposites. Significantly, the resultant nanomaterial exhibited excellent electrocatalytic stability and OER performance with a very low overpotential of only 212 mV at a current density of 10 mA cm^{-2} in O_2-saturated 1 M KOH solution, and low Tafel slope of 64.2 mV dec^{-1}, superior to that of IrO_2 and most previously reported $Ni(OH)_2$-based nanomaterials. Moreover, density functional calculation (DFT) further demonstrates that the interaction between embedded $Ni(OH)_2$ NPs and sulfur anions from CSZ plays a crucial role in improving OER.

RESULTS AND DISCUSSION

UCR-20-GaGeS-TAEA is one of the classical CSZs with the framework formula of $[Ga_{2.7}Ge_{1.3}S_8]^{2.7-}$ (TAEA is short for the template molecule of tris(2-aminoethyl)-amine).[36] Due to superior porosity and water stability among all previously reported crystalline CSZs, it is chosen as a suitable matrix for hosing the confined $Ni(OH)_2$ NPs. Unfortunately, the simple Ni^{2+}-exchanging process followed by base-solution-involved treatment can not effectively lead to the formation of large amount of $Ni(OH)_2$ NPs due to the charge limitation on the framework.. To embed more $Ni(OH)_2$ NPs in CSZ, a post-modification strategy, i.e. sequential fluoride-assisted cationic stripping and *in-situ* generation process, is designed based on the following consideration. According to hard and soft acid-base (HSAB) theory, the hard base F^- ions have stronger affinity to Ge^{4+} than soft base S^{2-} ions (See Supporting Information, Equation 5 and Table S1). In this work, sodium fluoride (NaF) was used as the stripping agent to extract partial Ge^{4+} ions from CSZ framework, which simultaneously makes some S^{2-} species escaped out of framework host (**Fig. S1**) and correspondingly increase the porosity of CSZ. In addition, the hydrolyzation of fluoride ions also provides OH^- species for the in-situ formation of $Ni(OH)_2$ NPs (**Fig. S2**). The detailed description can be seen in ***Supporting Information***. Finally, $Ni(OH)_2$ NPs@CSZ composite was successfully prepared *via* approach stated above by mixing the crystalline samples of CSZ (UCR-20-GaGeS-TAEA) with nickel chloride and 1 M NaF solution (**Scheme 1**).

The structure and mophology of several Ni^{2+}-treated CZSs were characterized by powder X-ray diffraction (PXRD), X-ray photoelectron spectroscopy (XPS), high resolution transmission electron microscopy (HRTEM), X-ray absorption near edge structure (XANES) and extended X-ray absorption fine structure (EXAFS) data. According to PXRD results in **Fig. S3-S5**, Ni@CSZ and $Ni(OH)_2$ NPs@CSZ displayed slightly shift towards higher angle in comparison with original CSZ, which may be contributed to the variation of unit cell parameter caused by the introduction of Ni^{2+} ions.[41] Some new PXRD peaks observed in $Ni(OH)_2$ NPs@CSZ were attributed to β-$Ni(OH)_2$ (PDF#-14-0117). Interestingly,

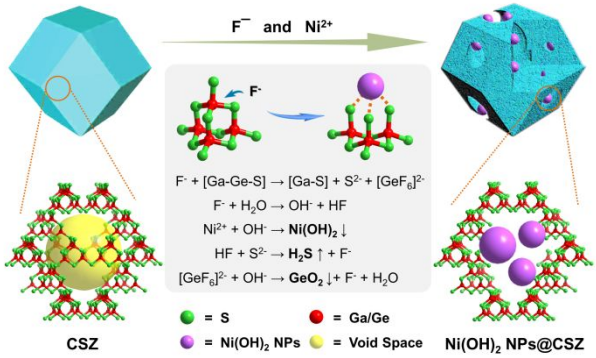

Scheme 1. The schematic about the formation of $Ni(OH)_2$ NPs@CSZ via sequential cation striping and in-situ generation processes under the presence of F^- and Ni^{2+} ions.

$Ni(OH)_2$ NPs@CSZ sample retained its original framework structure and even exhibited nickel atomic percentage three times higher than that of Ni@CSZ and a corresponding decrease in Ge/Ga ratio (**Fig. S6**). Notably, serious corrosion caused by excessive F^- anions could destroy the original framework structure, as exemplified in the sample of Ni@CSZ-NaF (2M), which exhibit similar PXRD pattern with $NaNiF_3$ (PDF#12-0219) (**Fig. S3 and S4**).

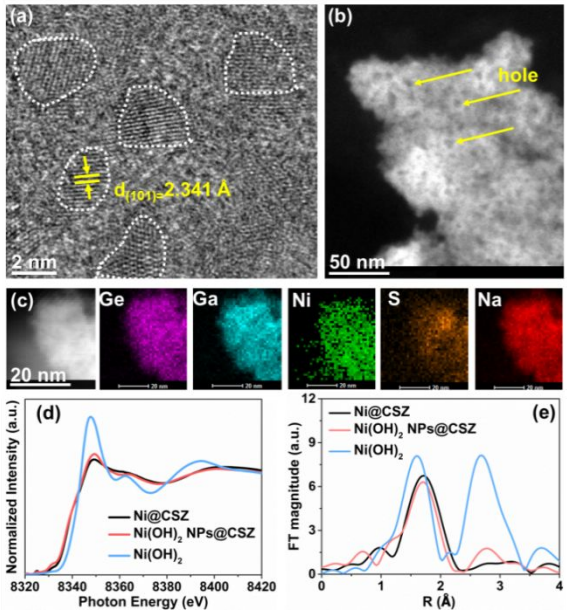

Fig. 1. (a) HRTEM image and the corresponding lattice fringes; (b) HAADF-STEM image (scale bare 50 nm); (c) HAADF-STEM image and the corresponding EDS elemental mapping images of $Ni(OH)_2$ NPs@CSZ solid sample treated by ultrathin sectioning; (d) normalized nickel K-edge XANES spectra; (e) Fourier transform curves of EXAFS.

The particle size of $Ni(OH)_2$ NPs in CSZ and their distribution were demonstrated by the high resolution transmission electron microscopy (HRTEM) with corresponding EDS mapping. TEM images in **Fig. S9c** showed that $Ni(OH)_2$ NPs confined in the etched CSZ were uniformly dispersed with an average size of ~3.3 nm, which can not be observed in Ni@CSZ and CSZ-NaF (**Fig. S9a-b**). The clear crystal lattice fringes of $Ni(OH)_2$ NPs with an interplanar spacing of 2.341 Å is ascribed to the (101)

crystal plane (**Fig. 1a**).[17] And abundant nickel compositions were observed to uniformly disperse in the whole crystal, as presented in the corresponding EDX mapping (**Fig. 1c**). Because of partial framework corrosion caused by F^--assisted cations stripping, mesoporous structures were observed in fluoride-treated CSZ through HAADF-STEM images (**Fig. 1b** and **Fig. S8**). The mesoporous structure in $Ni(OH)_2$ NPs@CSZ was further proved by the increased BET surface area, as displayed in N_2 sorption curves (**Fig. S7**). The formation of mesopore indirectly demonstrated that partial Ga/Ge-S bonds in the framework of CSZ were destroyed (**Fig. S1**). In addition, the good dispersity of $Ni(OH)_2$ NPs indicated that CSZ host can effectively inhibit the aggregation of NPs.

X-ray absorption near edge structure (XANES) measurements and extended X-ray absorption fine structure (EXAFS) measurements of the as-prepared materials and $Ni(OH)_2$ were performed to verify the coordination environment of Ni^{2+} or $Ni(OH)_2$ NPs in CSZ. As shown in the normalized nickel K-edge XANES spectra (**Fig. 1d**), both $Ni(OH)_2$ NPs@CSZ and Ni@CSZ display an edge energy at 8349 eV, which is similar to that for $Ni(OH)_2$ (8348 eV). By contrast, the Ni k-edge XANES spectra of $Ni(OH)_2$ NPs@CSZ and Ni@CSZ display blue shift, which might be attributed to the interaction between $Ni(OH)_2$ and S^{2-} from CSZ. In addition, **Fig. 1e** displays the EXAFS curves of $Ni(OH)_2$, $Ni(OH)_2$ NPs@CSZ and Ni@CSZ at Ni K-edge. For $Ni(OH)_2$ and $Ni(OH)_2$ NPs@CSZ, there are two obvious peaks within the range of 0.00-4.00 Å, in which the peak at 1.60-1.70 Å is attributed to Ni-O distance, while the second one in the range of 2.69-2.77 Å corresponds to the neighbouring Ni-Ni distance. The existence of Ni-Ni peak demonstrates that the as-synthesized $Ni(OH)_2$ NPs@CSZ composite includes abundant $Ni(OH)_2$ NPs. By contrast, only one peak at 1.70 Å (Ni-O) can be observed in Ni@CSZ. It is noteworthy that these peaks of Ni@CSZ (1.7 Å) and $Ni(OH)_2$ NPs@CSZ (1.7 Å and 2.7 Å) display obvious blue-shift compared with $Ni(OH)_2$ (1.6 Å and 2.69 Å), which locate between $Ni(OH)_2$ and NiS (1.86 Å for Ni-S and 2.93 Å for Ni-Ni distance) (**Fig. S10**). The phenomenon further reveals that the embedded free Ni^{2+} or $Ni(OH)_2$ NPs have some binding interaction with S^{2-} on CSZ. Therefore, strictly speaking, obtained NPs are S-doped $Ni(OH)_2$ NPs, which can be further confirmed by X-ray photoelectron spectra (XPS).

The chemical state and composition of as-prepared samples were further investigated *via* X-ray photoelectron spectroscopy (XPS). For Ni@CSZ and $Ni(OH)_2$ NPs@CSZ, C 1s, Ge 2p, Ga 2p, Ni 2p and S 2p signals can be clearly observed in XPS survey spectra (**Fig. S11**). However, Ge 2p, Ga 2p, and S 2p signals were hardly detected in Ni/CSZ-NaF (2M), suggesting that metal cations in substrate were striped completely by excessive F^- anions and converted into $NaNiF_3$ (**Fig. S4**). For S 2p in Ni@CSZ, two distinct peaks at 161.69 eV (S^{2-} $2p_{3/2}$) and 162.79 (S^{2-} $2p_{1/2}$) were observed (**Fig. 2a**).[38] However, for $Ni(OH)_2$ NPs@CSZ, besides these peaks located at 161.51 eV (S^{2-} $2p_{3/2}$) and 162.94 eV (S^{2-} $2p_{1/2}$), an extra peak located at 168.89 eV (S-O bond) was detected (**Fig. 2c**).[38, 42] The formation of S-O bond may be caused by the oxygenation of the dissociative S^{2-} from the destroyed framework. Similar S 2p peaks at 161.72 eV and 168.37 eV were observed in Ni/CSZ-NaF(2M) (**Fig. 2e**). As presented in **Fig. 2b**, two pair of fairly weak peaks were detected in Ni 2p spectra of Ni@CSZ, assigned to $2p_{1/2}$ (873.3 eV and its satellite (sat.) peak) and $2p_{3/2}$ (856.05 eV and its sat.) of Ni^{2+} ions. For $Ni(OH)_2$ NPs@CSZ, the corresponding peaks were also

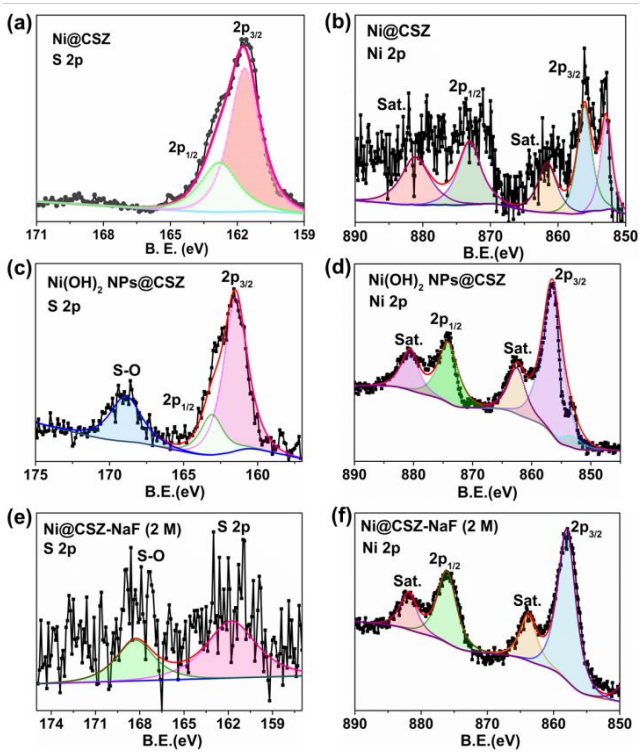

Fig. 2. XPS spectra of as-prepared materials: (a) S 2p and (b) Ni 2p in Ni@CSZ; (c) S 2p and (d) Ni 2p in $Ni(OH)_2$ NPs@CSZ; (e) S 2p and (f) Ni 2p in Ni/CSZ-NaF(2 M).

obviously observed at the binding energy of 856.5 eV (Ni $2p_{3/2}$) and 874.1 eV (Ni $2p_{1/2}$) with the distance of spin energy around 17.6 eV, indicating the existence of $Ni(OH)_2$ phase.[43] In addition, the weak Ni-S bond (853.2 eV) suggested the binding interaction between embedded $Ni(OH)_2$ NPs and sulfur from CSZ. Ni $2p_{3/2}$ (858.00 eV and its sat. peak) and Ni $2p_{1/2}$ (876.12 eV and its sat. peak) in Ni@CSZ-NaF (2 M) shift to higher binding energy, which is attributed to the formation of Ni-F bond (**Fig. 2f**).[44]

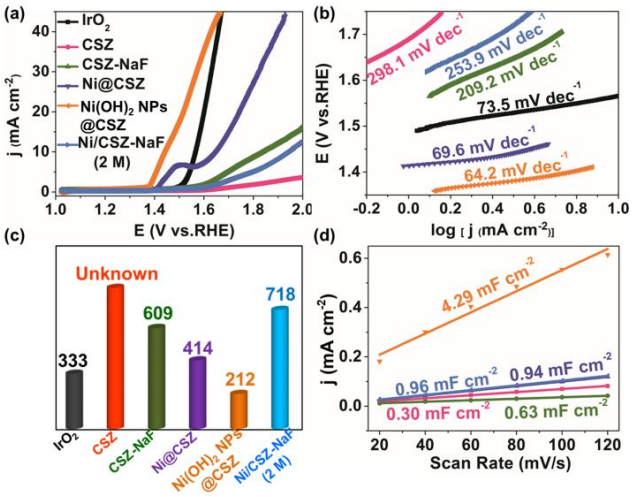

Fig. 3. (a) Linear sweep curves (LSV) of CSZ， CSZ-NaF, Ni@CSZ, $Ni(OH)_2$ NPs@CSZ and Ni/CSZ-NaF(2M) with 5 mV/s scan rate in O_2-statuated 1 M KOH solution; (b) the corresponding Tafel slope; (c) the histogram about the comparsion of overpotential at current density of 10 mA/cm^2; (d) Plots used for evaluating for Cdl of prepared samples.

The electrocatalytic activity of as-prepared materials was performed on typical three-electrode system in O_2-satuated 1 M KOH solution, in which catalysts were directly coated on glass carbon electrode (GCE) as working electrode. It should be noted that acetylene black (AB) was added to improve the conductivity of catalysts (**Fig. S28**). According to the linear sweep voltammetry (LSV) curves, catalysts obtained through Ni^{2+}-involved treatment on raw material of CSZ exhibited better OER activity than that of catalysts obtained from Cs^+-exchanged sample (Cs@CSZ) (**Fig. S12**). This is mainly caused by the supporting role of templated molecules of TAEA, which allow the sequential stripping and *in-situ* generation processes to be easily completed without original structure collapse. By contrast, Cs@CSZ sample was easily destroyed by NaF and Ni^{2+} ions (**Fig. S13**). As shown in **Fig. 3a-3c**, it was obviously observed that $Ni(OH)_2$ NPs@CSZ exhibited the best OER activity with a low overpotential of 212 mV at current density of 10 mA cm^{-2} and low Tafel slope of 64.2 mV dec^{-1}, which is superior to that of IrO_2, CSZ, CSZ-NaF, Ni@CSZ, Ni/CSZ-NaF(2M) and most previously reported $Ni(OH)_2$-based nanocatalysts (**Table S2**). It is noteworthy that small oxidation peak at ~1.4 V before oxygen evolution in Ni@CSZ can be obvious observed, which can be explained by electron transfer process (from Ni^{2+} to Ni^{3+}).[19, 28] The highly efficient OER activity of $Ni(OH)_2$ NPs@CSZ could be answered by abundant $Ni(OH)_2$ NPs active sites embedded in porous substrate of CSZ. Moreover, the LSV curves of $Ni(OH)_2$ NPs@CSZ-MF (1 M) (M = Li/Na/Cs) were performed to explore the effect of different stripping agents on catalytic activity. As presented in **Fig. S16**, $Ni(OH)_2$ NPs@CSZ-NaF (1M) exhibited superior catalytic activity than $Ni(OH)_2$ NPs@CSZ-CsF (1M) (η_{10} = 255 mV) and $Ni(OH)_2$ NPs@CSZ-LiF (1M) (η_{10} = 697 mV). This is caused by the different content of $Ni(OH)_2$ NPs (**Fig. S17 and S18**). When high-valent Ge/Ga cations were etched *via* cationic stripping, the corresponding framework possesses more negative charge than that of original CSZ. To balance the global charge of the framework, more positively-charged counter ions ($Cs^+/Li^+/Na^+/Ni^{2+}$) were introduced. Based on HSAB theory, the soft acid of Cs^+ could diffuse and bond with soft base of S^{2-} sites easily in the CSZ framework, compared to the hard acid of Li^+ and Na^+. However, among these elements, Cs^+ ion with the largest ionic radius (about 1.81~2.02 Å) to some extent could restrict the doping of more nickel, which could lower the OER performance. The electrode kinetics in OER process were explored via electrochemical impedance spectroscopy (EIS). As shown in **Fig. S14f and Fig. S15**, $Ni(OH)_2$ NPs@CSZ exhibited a minimum semicircle diameter, suggesting fast electron transfer kinetics. The electrocatalytic performance of $Ni(OH)_2$ NPs@CSZ was further compared by recording the electrochemical double layer capacitance (C_{dl}), which was performed by measuring cyclic voltammetry (CV) curves at different scan rates (**Fig. S14a-e**). The obtained C_{dl} was utilized to evaluate the electrochemical active surface area (ECSA). Clearly, $Ni(OH)_2$ NPs@CSZ displayed the largest value of C_{dl} (4.29 mF cm^{-2}), which suggested that it has larger ECSA than other catalysts. And, $Ni(OH)_2$ NPs@CSZ displayed superior stability (**Fig. S19 and S20**). The turnover frequency (TOF) was also calculated at overpotential of 300 mV in 1 M KOH solution. $Ni(OH)_2$ NPs@CSZ showed larger TOF of 0.026 s^{-1} than that of Ni@CSZ (0.022 s^{-1}) (**Fig. S21**).

In addition, to explore the stability of catalysts, PXRD, Raman, TEM, XPS measurements were performed on the catalysts after OER tests. The characterized peaks of CSZ and $Ni(OH)_2$ NPs were still observed in the PXRD of $Ni(OH)_2$ NPs@CSZ after OER (**Fig. S22**). However, the diffraction intensity of CSZ substrate became weaker, which demonstrates that may the stability of catalysts may be slightly affected by OER tests. Moreover, new NiOOH phase was observed, which contributed to the electron transfer between Ni^{2+} and Ni^{3+} during OER processes.[20, 21] This can be further confirmed by Raman spectrum (473 cm^{-1}) and HRTEM (**Fig. S23 and Fig. S27**).[45] In addition, the observed lattice fringe with interlayer distance of 2.087 Å was assigned to the (107) plane of $4Ni(OH)_2$-NiOOH, which indirectly confirmed the existence of NiOOH phase (**Fig. S23**). Interestingly, the distribution of NPs after OER tests is uniform and the corresponding size is still in the range of 2-4 nm (**Fig. S24**). To further understand the chemical composition and electronic state of $Ni(OH)_2$ NPs@CSZ after OER test, XPS measurements were performed (**Fig. S25**). The Ni 2p signals before and after OER is almost unchanged (**Fig. S25a**).The position of S 2p signals is almost unchanged, but the peak area ratio of S-O peak and S^{2-} changed obviously (**Fig. S25b**).

Density functional theory (DFT) calculations were performed to investigate the influence of dopant S on catalytic activity of the confined $Ni(OH)_2$ NPs. The model of S-doped β-$Ni(OH)_2$ is structurally simulated by substituting O on edge sites of β-$Ni(OH)_2$ with S. According to DFT results, the microscopic reaction mechanisms of the two models were proposed, which belong to typical four main sequential steps for OER (**Fig. 4a** and **Fig. S26**). The free energy profiles for the intermediates on β-$Ni(OH)_2$ and S-doped β-$Ni(OH)_2$ displayed the energy barrier for each reaction step, and these barriers were compared at different potential U (**Fig. 4b** and **Table S3-S6**). Based on calculated maximum energy barrier, the rate-determining step (RDS) of β-$Ni(OH)_2$ and S-doped β-$Ni(OH)_2$ is the conversion of OH* to O*, which is consistent with previously reported cases. For pristine β-$Ni(OH)_2$, the energy barrier of RDS is 2.346 eV. However, the value is significantly reduced into 2.116 eV in S-doped β-$Ni(OH)_2$, indicating that S dopants can effectively facilitate OER processes (**Fig. 4b**). The similar calculation results can be observed at other potential U. These results suggested that the S dopants in the embedded $Ni(OH)_2$ NPs play a crucial role in improving OER performance.

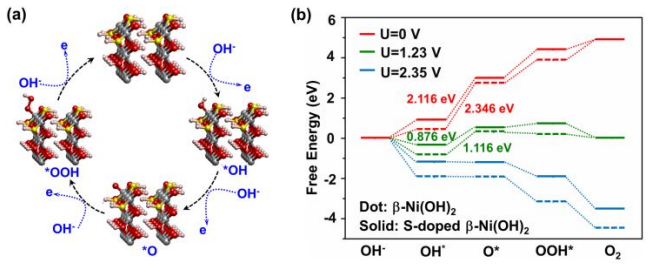

Fig. 4. (a) the most probable OER mechanisms on S-doped β-$Ni(OH)_2$ with octahedral Ni atom as active adsorption site; (b) the calculated free energies diagrams for OER of β-$Ni(OH)_2$ (Ni*) and S-doped β-$Ni(OH)_2$ (Ni*) at different potential U values.

CONCLUSIONS

In summary, we presented an effective strategy, *i.e.* sequential fluoride-assisted cationic stripping and in-situ generation processes, to successfully construct semiconductor-zeolite-confined $Ni(OH)_2$ NPs nanocomposite for highly efficient OER. As a proof-of-concept, the obtained material of $Ni(OH)_2$ NPs@CSZ exhibited excellent OER performance with a very low overpotential of only 212 mV at a current density of 10 mA cm^{-2} in O_2-saturated 1 M KOH solution, and low Tafel

slope of 64.2 mV dec^{-1}, superior to that of IrO_2 and most previously reported $Ni(OH)_2$-based composites. Density functional calculation (DFT) demonstrates the interaction between embedded $Ni(OH)_2$ NPs and sulfur sites from CSZ plays a crucial role in enhancing OER activity. This work demonstrates the modified metal-chalcogenide semiconducting open framework can be utilized as favorable substrate to load NPs with catalytic activity, and further facilitate their electrocatalytic performance.

ACKNOWLEDGEMENTS

The research was supported by the National Science Foundation (DMR-1506661, P. F.), the National Natural Science Foundation of China (21671142 and 21875150, T. W.), the Jiangsu Province Natural Science Fund for Distinguished Young Scholars (BK20160006, T. W.), the Project of Scientific and Technologic Infrastructure of Suzhou (SZS201905, T. W.) and the Priority Ac-ademic Program Development of Jiangsu Higher Education Institu-tions (PAPD). Dandan Hu acknowledges the support of the China Scholarship Council (CSC) for the living expenses in US.

AUTHOR INFORMATION

Corresponding Author

*E-mail: wutao@suda.edu.cn;
*E-mail: pingyun.feng@ucr.edu

Notes

The authors declare no competing financial interest.

REFERENCES

1 I. Roger, M.A. Shipman, M.D. Symes, *Nat. Rev. Chem.*, 2017, **1**, 1-13.
2 J.D. Blakemore, R.H. Crabtree, G.W. Brudvig, *Chem. Rev.*, 2015, **115**, 12974-13005.
3 H.A. El-Sayed, A. Wei, L.F. Olbrich, G.P. Putro, H.A. Gasteiger, *J. Electrochem. Soc.*, 2019, **166**, 458-464.
4 J. Gao, C.Q. Xu, S.F. Hung, W. Liu, W. Cai, Z. Zeng, C. Jia, H.M. Chen, H. Xiao, J. Li, Y. Huang, B. Liu, *J. Am. Chem. Soc.*, 2019, **141**, 3014-3023.
5 Z.W. Seh, J. Kibsgaard, C.F. Dickens, I. Chorkendorff, J.K. Norskov, T.F. Jaramillo, *Science*, 2017, **355**, 1-12.
6 C.N. Brodsky, A.P. Young, K.C. Ng, C.H. Kuo, C.K. Tsung, *ACS Nano*, 2014, **8**, 9368-9378.
7 Y. Pi, Q. Shao, P. Wang, J. Guo, X. Huang, *Adv. Funct. Mater.*, 2017, **27**, 1700886-1700894.
8 W. Zhou, D.D. Huang, Y.P. Wu, J. Zhao, T. Wu, J. Zhang, D.S. Li, C. Sun, P. Feng, X. Bu, *Angew. Chem. Int. Ed.*, 2019, **58**, 4227-4231.
9 L. Li, H. Yang, J. Miao, L. Zhang, H.-Y. Wang, Z. Zeng, W. Huang, X. Dong, B. Liu, *ACS Energy Lett.*, 2017, **2**, 294-300.
10 H.Y. Wang, S.F. Hung, H.Y. Chen, T.S. Chan, H.M. Chen, B. Liu, *J. Am. Chem. Soc.*, 2016, **138**, 36-39.
11 Y.J. Tang, C.H. Liu, W. Huang, X.L. Wang, L.Z. Dong, S.L. Li, Y.Q. Lan, *ACS Appl. Mater. Inter.*, 2017, **9**, 16977-16985.
12 H.B. Tao, L. Fang, J. Chen, H.B. Yang, J. Gao, J. Miao, S. Chen, B. Liu, *J. Am. Chem. Soc.*, 2016, **138**, 9978-9985.
13 Y. Zhang, Q. Shao, S. Long, X. Huang, *Nano Energy*, 2018, **45**, 448-455.
14 J. Xie, Y. Xie, *Chem.*, 2016, **22**, 3588-3598.
15 J. Yu, Y. Li, X. Long, S. Yang, J.K. Clark, M. Nakabayashi, N. Shibata, J.J. Delaunay, *ACS Catal.*, 2019, **9**, 1605–1611.
16 Y.-S. Xie, Z. Wang, M. Ju, X. Long, S. Yang, *Chem. Sci.*, 2019, **10**, 8354-8359.
17 X. Long, W. Qiu, Z. Wang, Y. Wang, S. Yang, *Mater. Today Chem.*, 2019, **11**, 16-28.
18 Z. Chen, Z. Wang, R. Cai, Y. Xie, J. Yu, X. Long, B. Yang, S. Yang, *Nanoscale*, 2020, **12**, 2472-2478.
19 C. Luan, G. Liu, Y. Liu, L. Yu, Y. Wang, Y. Xiao, H. Qiao, X. Dai, X. Zhang, *ACS Nano*, 2018, **12**, 3875-3885.
20 S. Anantharaj, P. E. Karthik, S. Kundu, *Catal. Sci. Technol.*, 2017, **7**, 882-894.
21 P. Tian, Y. Yu, X. Yin, X. Wang, *Nanoscale*, 2018, **10**, 5054-5059.
22 X. Guo, R.-M. Kong, X. Zhang, H. Du, F. Qu, *ACS Catal.*, 2017, **8**, 651-655.
23 X. Zhao, X. Ding, Y. Xia, X. Jiao, D. Chen, *ACS Appl. Nano Mater.*, 2018, **1**, 1476-1483.
24 K. Zhu, H. Liu, M. Li, X. Li, J. Wang, X. Zhu, W. Yang *J. Mater. Chem. A*, 2017, **5**, 7753-7759.
25 J. Yan, L. Kong, Y. Ji, J. White, Y. Li, J. Zhang, P. An, S. Liu, S.T. Lee, T. Ma, *Nat. Commun.*, 2019, **10**, 2149-2159.
26 Z. Zhang, T. Zhang, J.Y. Lee, *ACS Appl. Nano Mater.*, 2018, **1**, 751-758.
27 X. Zhu, X. Dou, J. Dai, X. An, Y. Guo, L. Zhang, S. Tao, J. Zhao, W. Chu, X.C. Zeng, C. Wu, Y. Xie, *Angew. Chem. Int. Ed.*, 2016, **55**, 12465-12469.
28 Z. Liu, N. Li, H. Zhao, Y. Zhang, Y. Huang, Z. Yin, Y. Du, *Chem. Sci.*, 2017, **8**, 3211-3218.
29 T. Kou, S. Wang, J.L. Hauser, M. Chen, S.R.J. Oliver, Y. Ye, J. Guo, Y. Li, *ACS Energy Lett.*, 2019, **4**, 622-628.
30 L. Wang, C. Lin, D. Huang, F. Zhang, M. Wang, J. Jin, *ACS Appl. Mater. Inter.*, 2014, **6**, 10172-10180.
31 O. Diaz-Morales, I. Ledezma-Yanez, M.T.M. Koper, F. Calle-Vallejo, *ACS Catal.*, 2015, **5**, 5380-5387.
32 Y. Rao, Y. Wang, H. Ning, P. Li, M. Wu, *ACS Appl. Mater. Inter.*, 2016, **8**, 33601-33607.
33 J. Xie, X. Zhang, H. Zhang, J. Zhang, S. Li, R. Wang, B. Pan, Y. Xie, *Adv. Mater.*, 2017, **29**, 1604765-1604774.
34 X.B. Han, X.Y. Tang, Y. Lin, E. Gracia-Espino, S.G. Liu, H.W. Liang, G.Z. Hu, X.J. Zhao, H.G. Liao, Y.Z. Tan, T. Wagberg, S.Y. Xie, L.S. Zheng, *J. Am. Chem. Soc.*, 2019, **141**, 232-239.
35 Z. Xing, L. Gan, J. Wang, X. Yang, *J. Mater. Chem. A*, 2017, **5**, 7744-7749.
36 X.Bu, N. Zheng, B. Wang, P. Feng, *Science*, 2002, **298**, 2366-2369.
37 D.-D. Hu, J. Lin, Q. Zhang, J.-N. Lu, X.-Y. Wang, Y.-W. Wang, F. Bu, L.-F. Ding, L. Wang, T. Wu, *Chem. Mater.*, 2015, **27**, 4099-4104.

38 D. Hu, X. Wang, H. Yang, D. Liu, Y. Wang, J. Guo, T. Wu, *Electrochim. Acta*, 2018, **282**, 877-885.
39 S. Niu, W.J. Jiang, T. Tang, Y. Zhang, J.H. Li, J.S. Hu, *Adv. Sci.*, 2017, **4**, 1700084-1700090.
40 A. Balram, H. Zhang, S. Santhanagopalan, *Mater. Chem. Front.,*, 2017, **1**, 2376-2383.
41 W.Q. Zaman, W. Sun, M. Tariq, Z. Zhou, U. Farooq, Z. Abbas, L. Cao, J. Yang, *Appl. Catal. B-Environ*, 2019, **244**, 295-302.
42 X. Du, Z. Yang, Y. Li, Y. Gong, M.Zhao, *J. Mater. Chem. A*, 2018, **6**, 6938-6947.
43 L. Zhang, I.S. Amiinu, X. Ren, Z. Liu, G. Du, A.M. Asiri, B. Zheng, X. Sun, *Inorg. Chem.*, 2017, **56**, 13651-13654.
44 B. Zhang, K. Jiang, H. Wang, S. Hu, *Nano Lett.*, 2019, **19**, 530-537.
45. K. S. Joya, X, Sala, *Phys. Chem. Chem. Phys.,* 2015, **17**, 21094--21103